iScience

Article

Decoupling CO_2 effects from electrochemistry: A mechanistic study of copper catalyst degradation

Graphical abstract

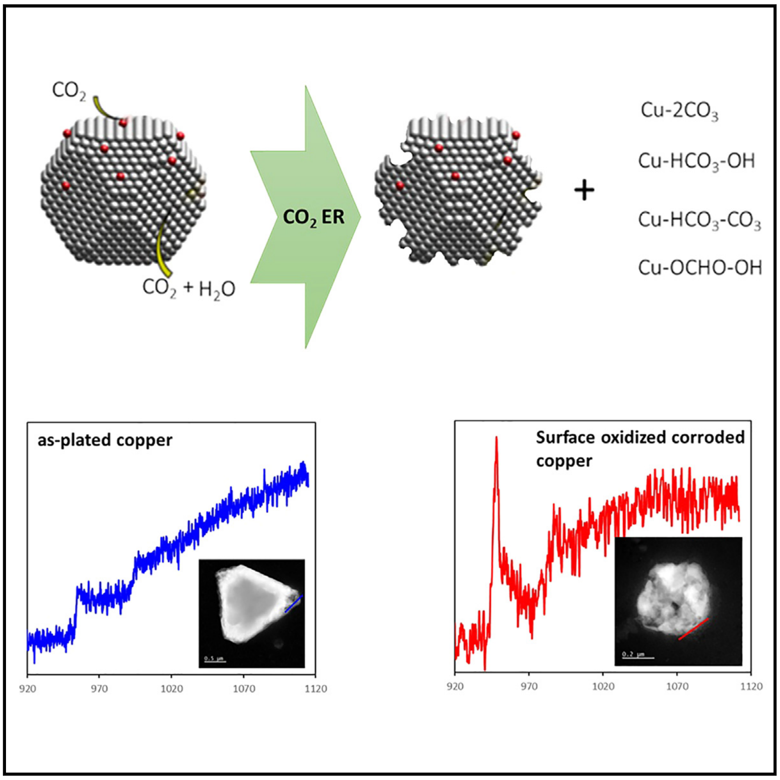

Authors

Rui Serra-Maia, Joel B. Varley, Stephen E. Weitzner, ..., Jurgen Biener, Sneha A. Akhade, Eric A. Stach

Correspondence

rui.maia@inl.int (R.S.-M.),
akhade1@llnl.gov (S.A.A.),
stach@seas.upenn.edu (E.A.S.)

In brief

Electrochemistry; Engineering; Materials science

Highlights

- Copper degradation in the presence of CO_2 can proceed without CO_2 ER
- Copper degradation does not happen without CO_2 even at E_{WE} capable of driving CO_2 ER
- *S*urface copper species are prone to dissolution in the presence of CO_2

Serra-Maia et al., 2025, iScience *28*, 111851
March 21, 2025
https://doi.org/10.1016/j.isci.2025.111851

CellPress

iScience

CellPress OPEN ACCESS

Article

Decoupling CO_2 effects from electrochemistry: A mechanistic study of copper catalyst degradation

Rui Serra-Maia,[1,*] Joel B. Varley,[2] Stephen E. Weitzner,[2] Henry Yu,[2] Rongpei Shi,[2] Jurgen Biener,[2] Sneha A. Akhade,[2,*] and Eric A. Stach[1,3,4,*]

[1]Department of Materials Science and Engineering, University of Pennsylvania, Philadelphia, PA 19104, USA

[2]Materials Sciences Division, Lawrence Livermore National Laboratory, Livermore, CA 94550, USA

[3]Laboratory for Research on the Structure of Matter, University of Pennsylvania, Philadelphia, PA 19104, USA

[4]Lead contact

*Correspondence: rui.maia@inl.int (R.S.-M.), akhade1@llnl.gov (S.A.A.), stach@seas.upenn.edu (E.A.S.)

https://doi.org/10.1016/j.isci.2025.111851

SUMMARY

Copper-based nanoparticles are key electrocatalysts for CO_2 electrochemical reduction (CO_2 ER) to liquid fuels and other value-added products. However, the copper catalyst can undergo rapid electrochemical corrosion, leading to a loss of catalyst material, fluctuations in the reaction conditions and increasing operational costs. We establish a mechanistic understanding of this detrimental process using *in situ* electrochemical electron microscopy and density functional theory (DFT). We find that copper corrosion can occur in the presence of CO_2 in electroless conditions and before the onset potentials required for CO_2 ER. The effects are isolated from pH changes resulting from dissolved CO_2. Particles of corroded copper have oxidized surfaces, in contrast to copper surfaces exposed to CO_2-free electrolytes. DFT calculations identify multiple routes by which CO_2 can behave as a dissolution agent for copper and copper-oxide surfaces and suggest that formate-intermediates are a key driver of corrosion. This study highlights microenvironment-based factors that affect copper performance and degradation, facilitating strategies to inhibit and reverse copper degradation during CO_2 ER.

INTRODUCTION

Renewable energy is increasingly abundant and future investment will allow it to meet the growing energy demand in the world.[1–4] A critical component for replacing fossil fuels with renewable energy is converting electrical power obtained from renewable sources into synthetic fuels that can be used in transportation or stored to be used on demand.[5,6] Reducing CO_2 into value-added products would produce synthetic fuels or commodity synthetic hydrocarbon molecules, while simultaneously contributing to reduce atmospheric CO_2 through carbon capture and utilization.[7–9]

Electrochemical CO_2 reduction (CO_2 ER) is an efficient and clean process to convert CO_2 into liquid fuels and other reduced carbon-based compounds.[9–13] In contrast with conventional commercial methods, such as CO_2 hydrogenation or the Fischer–Tropsch processes, CO_2 ER can be conducted under ambient temperatures and pressures using modular, scalable, and decentralized units.[14] Copper-based catalysts are the most selective materials known to unlock CO_2 ER toward C_{2+} compounds, such as ethanol and ethylene[10,15–17] and other multi-carbon hydrocarbons. And compared to other metal catalysts, copper exhibits a relatively lower selectivity toward hydrogen evolution, leading to unmatched Faradaic efficiencies for CO_2 ER.[18]

In the last two decades, numerous studies[19–21] attempted to optimize the catalytic activity, the energy efficiency, and the selectivity of copper. However, the stability of copper electrocatalysts is very poor—at most in the range of hundreds of hours—which is orders of magnitude lower than the timescales of industrial significance for comparative catalyst technologies, which exceed 30,000 h.[20] Studies have recently highlighted that this critical issue remains unresolved.[20]

The rapid degradation of copper-based cathodic catalysts under CO_2 ER affects their activity, selectivity, and overall performance.[22] The selectivity toward CO_2-reduced products lowers over time and hydrogen evolution becomes the prevalent reaction 10–30 min into the reaction.[23–25] The fundamental drivers of those changes are not well understood. DeWulf and coworkers produced methane and ethylene with 65% selectivity using copper foil but reported a selectivity drop to 0% after 2 h, which was correlated to the accumulation of carbon and graphitic species at the catalyst surface.[26] Similar results were also obtained for rotating-disk copper electrodes.[27–30] Copper deactivation during CO_2 ER was initially attributed to accumulation of metal impurities. Later, surface sensitive chemical techniques such as X-ray photoelectron spectroscopy (XPS), showed that the deposition of metal impurities on the electrode surface was not the main deactivation phenomenon.

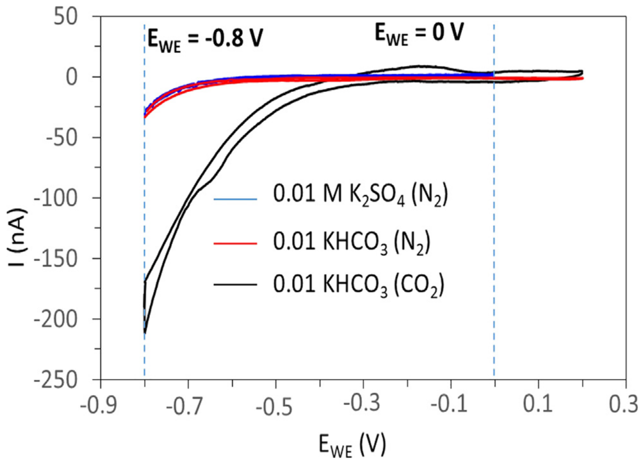

Figure 1. Cyclic voltammetry (first scan) of electroplated copper obtained for -0.8 V < E_{WE} vs. SHE' < 0.2 V after introducing different CO_2 ER electrolytes into the cell

Voltammetry on deactivated Cu electrodes showed unaccounted-for peaks at approximately -0.1 or -0.56 V versus Standard Hyrdogen Electrode (SHE). The extent of deactivation correlated with the electric charge of the anodic peak, which was interpreted as a correlation with the concentration of deactivation species.[22] In highly cathodic conditions, the corrosion of copper nanocubes was induced by alkali cations.[31] Huang and co-workers observed detachment of small clusters and pitting corrosion in copper nanocubes subjected to CO_2 ER using transmission electron microscopy (TEM) techniques.[32] The degradation of a Cu-based catalyst into 2–4 nm densely packed nanoparticles was also observed on an ethylene-selective copper catalyst.[30] The results suggested that morphological changes and corrosion were linked to the strong cathodic potential and formation of complexes with oxidized metastable carbon species. The authors identified *in situ* electron microscopy as a key tool to gain new insights and address unresolved questions of copper degradation during CO_2 ER.[20,33] Collectively, these studies underscore the fact that significant advances are needed to accurately identify and understand the mechanisms and agents by which copper degradation is promoted under electrochemical conditions. Uncovering the basis of degradation requires tightly coupled experiment-theory integration to obtain mechanistic understanding of the factors contributing to variations in the material performance.

In this work, we show that CO_2 plays a primary role in the degradation of copper during the CO_2 ER. We conduct systematic investigations of the various microenvironment factors contributing to copper degradation toward decoupling the electrolyte composition, the solution pH, the applied electrochemical potential, and the presence/absence of CO_2. Based on *in situ* experimental observations and first-principles calculations, we propose that the oxidized and unoxidized surface copper atoms can form complexes with CO_2 depending on the electrode potential. This causes corrosion, preferentially along lower-coordinated surface sites. These results provide insights needed to inhibit copper corrosion and develop highly stable copper-based catalysts that can withstand longer operational times for CO_2 ER or other electrochemical reactions.

RESULTS

Copper catalysts

The copper particles plated onto the indium tin oxide (ITO) electrode in this study were heterogeneous and representative of a real-world catalyst (Figure S4). A significant number of particles were faceted. The most prevalent particle facet families were the <100> and <111> (Figure S5). The heterogeneous morphology of the electroplated copper particles is linked to their electrodeposition within confined volumes, influenced by minor hydrodynamic fluctuations and substrate imperfections (Figure S6). This is a difference from several previous works that evaluated the stability of copper nanoparticles with well-defined size and morphology.[34–37]

Electrochemical copper activity for CO_2 ER

Electroplated copper shows CO_2 ER activity in 0.01 M $KHCO_3$ saturated with CO_2 at $E_{WE} < -0.3$ V vs. SHE' (Figure 1). The ITO electrode is inert at this range of electrochemical potentials, which means that the copper particles are responsible for this activity (Figure S1). On the contrary, copper only exhibited measurable electrochemical activity at $E_{WE} < -0.6$ V in 0.01 M K_2SO_4 saturated with N_2. K_2SO_4 saturated with N_2 is CO_2-free, which suggests that the detected activity is ascribed to the hydrogen evolution reaction (HER). The electrochemical activity of copper in 0.01 M $KHCO_3$ saturated with N_2 is equivalent to that observed in 0.01 M K_2SO_4 saturated with N_2. That indicates that the HER is also the predominant reaction when N_2 is bubbled into a 0.01 M $KHCO_3$ electrolyte.

Copper degradation during CO_2 ER

The susceptibility of electroplated copper to degradation during CO_2 ER was analyzed through *in situ* morphological analysis after 15 min (Figure 2). Copper subjected to $E_{WE} = -0.8$ V showed degradation pits (red arrows) in 0.01 M $KHCO_3$ saturated with CO_2, which is below (*in aliis verbis,* more reducing than) the onset potential for CO_2 ER and HER. These results show that copper is prone to degradation at -0.8 V, even though at standard conditions, this electrochemical potential would strongly favor copper plating. This is shown clearly by the pits and crevices that are visible in copper particles that were originally plated onto the electrode surface (Figure 2B). Within these confined spaces, the hydrodynamic and chemical conditions may diverge from those in the bulk, potentially leading to chemical reactions occurring outside the anticipated electrochemical potential range for a given redox pair.[37] On the contrary, copper did not exhibit signs of degradation at the same potential if 0.01 M K_2SO_4 or 0.01 M $KHCO_3$ were saturated with N_2 instead of CO_2 (Figures 2D and 2F).

Morphological analyses of copper particles subjected to CO_2 ER conditions in 0.01 M $KHCO_3$ saturated with CO_2 show surface roughening, pitting, and crevice degradation akin to corrosion observed in typical copper applications such as plumbing.[15,22,38–43] Preferential degradation was observed along grain boundaries, which formed crevices on the particles

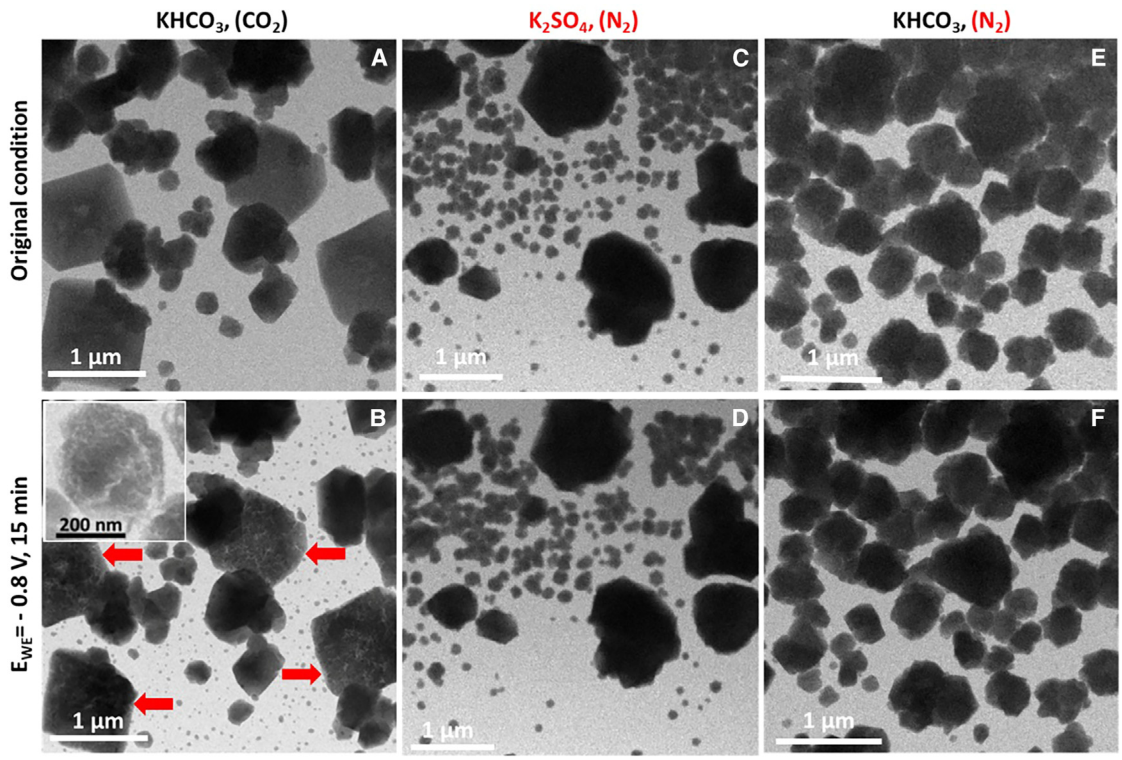

Figure 2. Copper corrosion at E_{WE} = −0.8 V vs. SHE' for 15 min

(A and B) In 0.01 M $KHCO_3$ saturated with CO_2, (C and D) in 0.01 M K_2SO_4 saturated with N_2, (E and F) in 0.01 M $KHCO_3$ saturated with N_2. Inset of (B) shows a high magnification image of a corroded Cu particle.

(Figure 3). This result is corroborated by the fact that larger particles, which contain more surface defects/grain boundaries, seem to be more susceptible to corrosion. The fine white lines meandering through the particle shown in Figure 3B indicate localized corrosion, likely following grain boundaries and other defects that locally destabilize Cu. The confinement created by these defects appears to accelerate the corrosion of Cu, possibly leading to crevice corrosion. That copper particle exhibits structural defects that already were present, at least in a small extent, in the as-plated particle (Figure 3C). This observation corroborates the relation between enhanced degradation and the presence of structural defects that facilitate crevice corrosion. At E_{WE} = −0.8 V, the degradation of the large particles was accompanied by the formation of the smaller re-plated copper nanoparticles. The re-plating of smaller nanoparticles was observed for potentials more reducing than E_{WE} = 0 V vs. SHE'.

The bulk of both the degraded and the re-plated particles is composed of metallic copper as revealed by electron energy loss spectroscopy (EELS), which is identical to the EELS signature for the as-plated copper particles before they were subjected to CO_2 ER conditions (Figure S7). The results are different when analyzing the surface of the particles. Copper particles that degraded when subjected to CO_2 ER exhibit an EELS signature for oxidized copper at the surface (Figure 3).[44,45] This contrasts with as-plated and re-precipitated copper particles, which exhibit an EELS signature for metallic copper, even at the surface (Figure S7). These results suggest that CO_2 may be playing either a direct or indirect role in copper degradation process. Therefore, an important question to resolve is whether degradation was induced by CO_2 itself, CO_2 ER products or a combination of both.

CO_2 induced copper corrosion

To gain insights into how CO_2 contributes to the degradation of copper under CO_2 ER conditions, we tested the susceptibility to degradation at potentials more anodic than the onset for CO_2 ER. This effectively removes CO_2 reduction products as possible causes for Cu degradation. Copper degradation did occur in $KHCO_3$ saturated with CO_2 at E_{WE} = 0 V vs. SHE' (Figures 4 and S8). This electrochemical potential is insufficient to drive CO_2 ER, which indicates that copper degradation is enabled even in the absence of CO_2 ER and its products. Interestingly, once again, at E_{WE} = 0 V copper degradation was only observed if CO_2 was present in the electrolyte, with the phenomena visibly being similar to that observed at E_{WE} = −0.8 V. An identical result was also observed for bulk copper, prepared through e-beam deposition. Even though this sample contained a bulk copper electrode, corrosion was still visibly evident after 15 min when $KHCO_3$ was saturated with CO_2 (Figures 4G and 4H).

We further investigated if the cause of copper corrosion in CO_2-saturated electrolyte solution was pH induced. The pH of the $KHCO_3$ electrolyte was recorded to be 5 when CO_2-saturated and 7 when saturated with N_2. We used 0.01 M H_2SO_4 to adjust the pH of $KHCO_3$ electrolyte saturated with N_2 to a

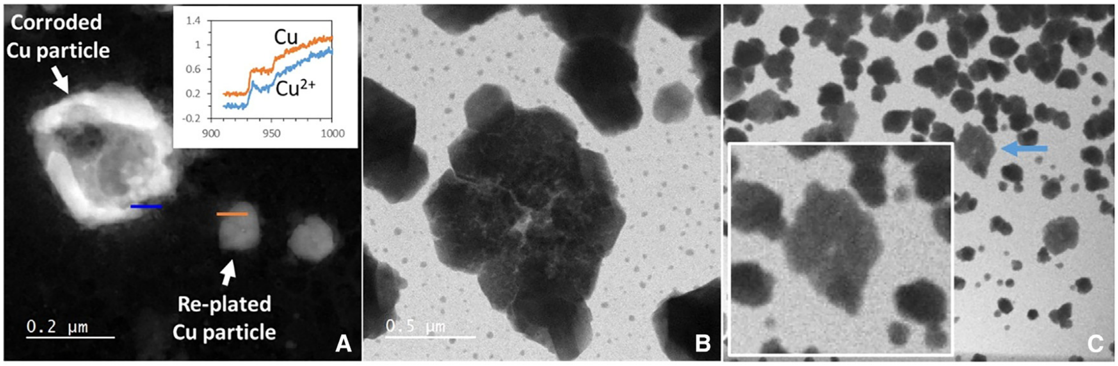

Figure 3. Chemical and structural analysis of copper subjected to E_{WE} = 0 V vs. SHE' in $KHCO_3$ (CO_2)

(A) Electron energy loss spectroscopy of a degraded and a re-plated copper particle.

(B) High-magnification analysis of a degraded and re-plated small copper particles showing that degraded particles exhibit preferential corrosion along structural defects.

(C) Low-magnification of the area with the as-plated copper particle analyzed in (B). Inset shows a magnified image of the same particle with a visible defect in the middle of the particle.

pH = 5. Similar to what was observed when the pH was not adjusted, no copper degradation was observed when the pH of an N_2 saturated 0.01 M $KHCO_3$ electrolyte was adjusted to 5. This eliminated pH as a likely cause for copper degradation when CO_2 instead of N_2 is bubbled into the electrolyte.

In summary, the results show that CO_2 itself, rather than a product of its electrochemical reduction or its influence on pH through carbonate buffer reactions, plays a key role in the degradation of copper during CO_2 ER. Copper degradation is observed as long as CO_2 is present, even if the applied electrochemical potential is insufficient to drive CO_2 electroreduction. In contrast, if CO_2 is not present, copper does not corrode, even at applied potentials that are sufficient to drive CO_2 ER.

Copper corrosion in electro-less conditions

To further understand the variables that control copper corrosion during the CO_2 ER and decouple the role of the applied potential in promoting and controlling copper degradation, we evaluated the stability of copper subjected to electro-less conditions (Figure 5).

Similar to the results observed for $E_{WE} = -0.8$ V or E_{WE} = 0 V, copper degradation occurred in electro-less conditions when $KHCO_3$ saturated with CO_2 was used, even for different electrolyte concentrations (Figures 5A–5D). Once again, no degradation was observed when $KHCO_3$ saturated with N_2 instead of CO_2 was used (Figures 5E and 5F). The degradation of copper in electro-less conditions observed here is corroborated by the fact that detached copper islets in the bulk copper sample also corroded, even though they were not connected to the electroactive copper electrode (Figures 4G and 4H).

Overall, these results indicate that CO_2 itself plays a crucial role in copper degradation, and that no electrochemical current or products of CO_2 ER are necessary for copper degradation to occur. Furthermore, increasing $KHCO_3$ electrolyte concentration by a factor of 10, from 0.01 M to 0.1 M, did not affect the Cu corrosion behavior under electroless conditions (Figure 5). This observation is consistent with a degradation mechanism that does not depend on K^+ or $HCO3^-$. Degradation was fast at less reducing electrochemical potentials, when the driving force for copper plating is smaller, which is consistent with the rapid degradation observed on the separate islets (that should exhibit no plating forces at open-circuit conditions) in the bulk copper sample compared to the part of the sample that was under E_{WE} = 0 V. At more negative electrochemical potentials, only larger particles show corrosion, but at less negative potentials both large and small particles exhibit corrosion.

Ab initio calculations

To rationalize how the corrosion of copper observed in this study was linked to its interaction with CO_2 in the electrolyte, we performed *ab initio* calculations that analyzed the ability of surface copper to interact and form complexes with chemical species present in the electrolyte.

Cu degradation susceptibility was estimated by calculating the thermodynamic driving force for electrodissolution under varying electrochemical conditions. The potential-dependent copper vacancy formation energies and the corresponding copper dissolution potentials are summarized in Figure 6 for the most favorable of the studied set of solvated copper complexes, which include various combinations of OH, CO_3, HCO_3, CO_2, OCHO, and H_2O ligands as detailed in the supplemental information.

The vacancy formation energies correlate with the site coordination number, with V_{Cu} predicted to form more easily on lower coordinated binding sites such as step edges on the (211) surfaces over higher-coordinated sites like on (100) and (111) terraces. The solvated copper complexes with one or more hydroxide ligands are generally found to be the most favorable, exhibiting the largest thermodynamic driving force toward forming surface vacancies and facilitating degradation on the copper surface. As seen in Figure 6A, $Cu(OH)_2$ formation has calculated dissolution potentials that are -1.02 V vs. SHE (-0.61 V vs. RHE) for Cu(211) step edges and ~0.3–0.5 V higher on terraces, indicating that Cu dissolution is thermodynamically favorable under

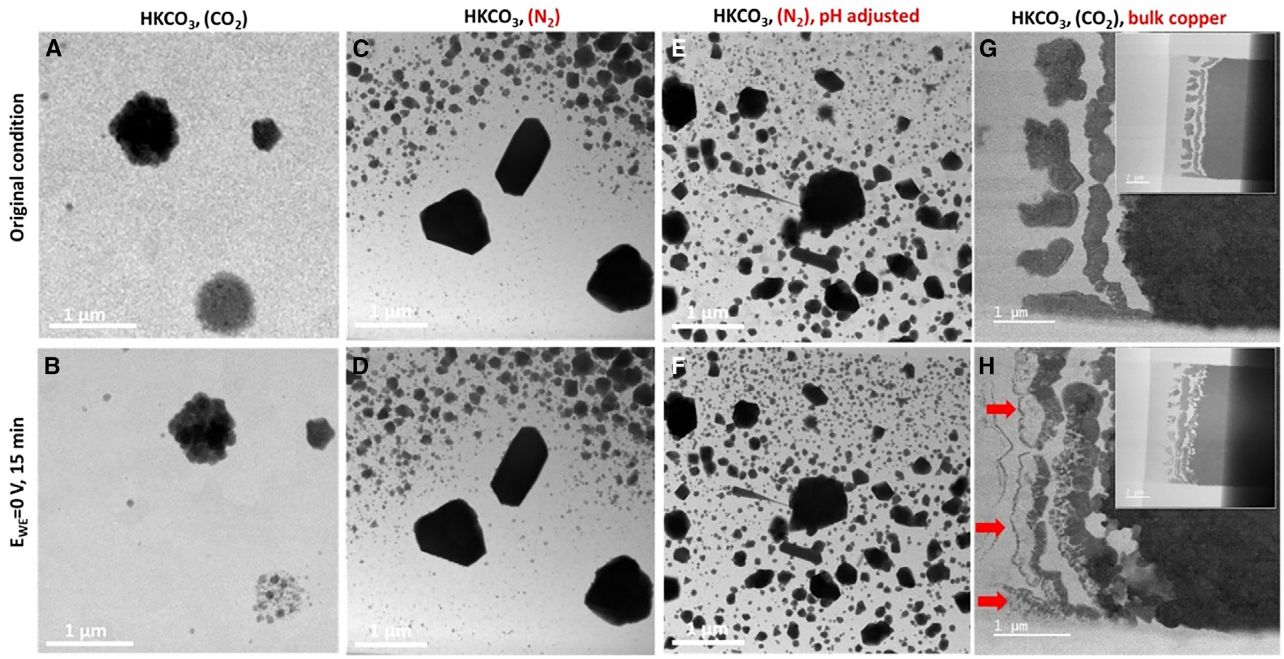

Figure 4. Copper corrosion below the onset for CO_2 ER (E_{WE} = 0 V vs. SHE') for 15 min

(A and B) In 0.01 M $KHCO_3$ saturated with CO_2, (C and D) in 0.01 M $KHCO_3$ saturated with N_2, (E and F) in 0.01 M $KHCO_3$ saturated with N_2 and pH adjusted to 5, (G and H) in 0.01 M $KHCO_3$ saturated with CO_2 using a bulk copper electrode.

modestly reducing potentials consistent with CO_2 ER. We note that these dissolution potentials also depend on pH, the ionic strength, and the concentration of Cu in solution ([Cu]), which can further alter the specific potential values at which Cu dissolution is expected to become thermodynamically preferable. In Figure 7 we include the pH dependence of the most favorable complexes for each Cu facet, all assuming the same [Cu] as in Figure 6.

While the formation of dissolved $Cu(OH)_2$ complexes appears feasible under the studied applied potentials, this dissolution route does not require the presence of CO_2, which suggests other pathways for Cu dissolution must be contributing under CO_2 ER conditions based on the experimental observations. For applied potentials below the onset of CO_2 reduction, CO_2 binding can result in OCHO* intermediates on Cu,[46] while CO_2 binding on oxidized copper surfaces can lead to the presence of CO_3 and HCO_3-like bound intermediates.[47,48] The dissolution of Cu via these types of complexes are included in Figures 6B–6D, in Figure 7 and in the supplemental information, where we find that at studied pH and applied potential ranges, complexes with OCHO and OH exhibit the most reducing dissolution potentials. For example, we calculate dissolution potentials of −0.54 V vs. SHE (−0.13 vs. RHE) on Cu (211) step edges with the formation of Cu-OCHO-OH complexes (Figure 6D). We also find that Cu-2CO_3, Cu-HCO_3-OH, and Cu-HCO_3-CO_3 complexes can also facilitate surface degradation at less reducing potentials (see Figure 7), but these generally require higher pHs than accessed in our *in situ* measurements. Nonetheless, our calculated values indicate that a number of these complexes can thermodynamically initiate surface degradation in the range of electrochemical potential values tested experimentally in this study. The detrimental role of OCHO* in dissolution is consistent with experiments performed at near-neutral pH values, the presence of CO_2 in solution, and low reducing potentials before CO_2 ER is initiated. We also expect that the thermodynamic dissolution potentials to be lower for nanoparticles with higher surface roughness that contain undercoordinated copper atoms at defect, kink, or edge sites.

DISCUSSION

Our results suggest that at low pH the well-known copper degradation observed during CO_2 ER is a corrosion process that depends on the presence of CO_2 in solution, even if the CO_2 ER reaction is not being driven. This contrasts with previous studies that report copper fragmentation during CO_2 ER induced by applied electrochemical potentials.[15,20,49–51] Likewise, if Cu corrosion was induced by alkali metal cations, such as K^+, as some recent studies have suggested, one would expect copper to corrode even when $KHCO_3$ or K_2SO_4 were saturated with N_2, which is contradicted by our results, even at very cathodic potentials.[31] Similar to other metals of the ninth column and the top row of the transition metals, copper too can form a variety of CO_2-containing charged complexes which can be mobilized into aqueous media (solubilization).[52] Indeed, this is a risk associated with CO_2 injection into underground aquifers for carbon sequestration purposes, where Cu and other metals can form carbonates and become mobilized in solution.[53] The degradation of copper when CO_2 is present in solution, whether CO_2 ER is happening or not, is also consistent with copper corrosion

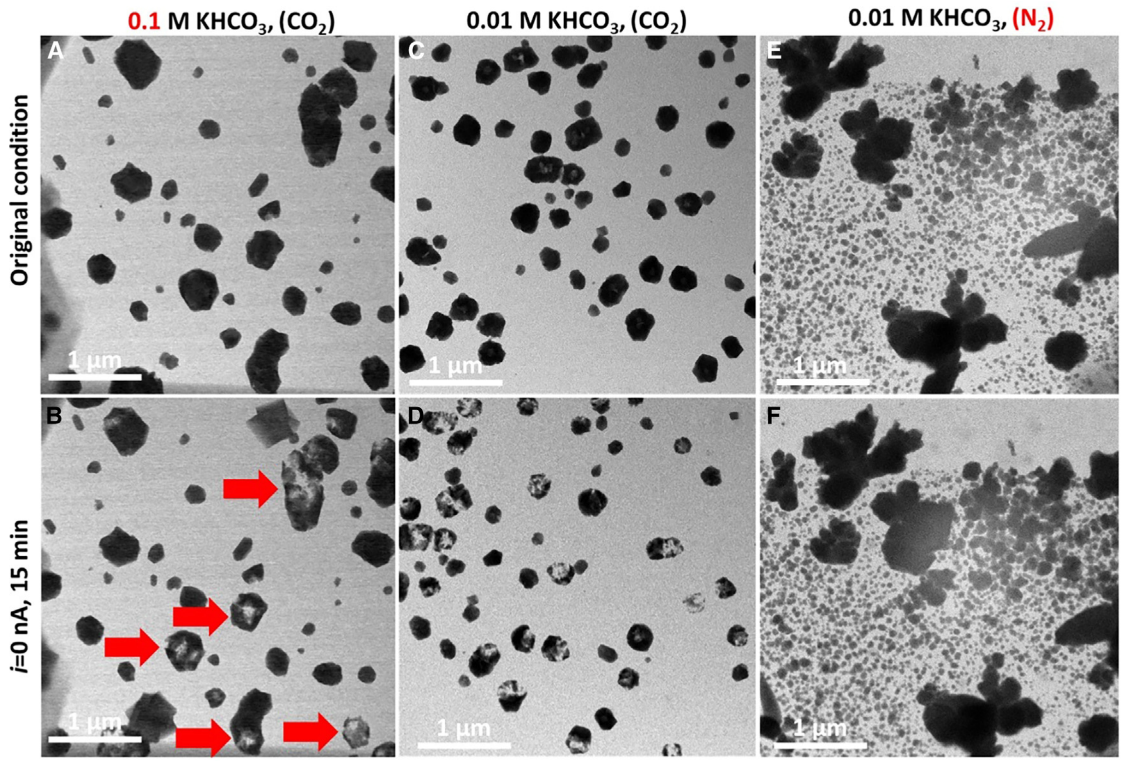

Figure 5. Copper corrosion in electro-less conditions (i = 0 nA) for 15 min

(A and B) In 0.1 M $KHCO_3$ saturated with CO_2, (C and D) in 0.01 M $KHCO_3$ saturated with CO_2, (E and F) in 0.01 M $KHCO_3$ saturated with N_2.

caused by acid rain, where CO_2 acts as a corrosion agent.[52,54,55] The role of CO_2 in the corrosion of copper is supported by the lack of observed degradation when $KHCO_3$ is saturated with N_2 instead of CO_2. CO_2 can interact directly with Cu surfaces, via O and OH to form CO_3 and HCO_3 species that may facilitate the Cu dissolution process.[48] This is supported by the oxidized copper signature shown in the EELS results for Cu particles that undergo degradation. Both our experimental results and our DFT calculations suggest that surface complexed copper is prone to be pulled into solution in the presence of CO_2, thus supporting a corrosion driven degradation. This supports our conjecture that HCO_3^- or metal cations by themselves do not have an active role in the Cu corrosion process, but that a CO_2 saturated $KHCO_3$ electrolyte is an intrinsically corrosive environment for Cu.

If copper degradation required CO_2 ER, one would expect the degradation kinetics to correlate with the electrochemical potential applied, which is contrary to what is observed.[15,20,50,51] The enhanced degradation observed for larger copper particles is consistent with an increase in the local pH due to a parasitic hydrogen evolution reaction. Larger particles have more catalytic sites consuming hydrogen ions, which exacerbates the increase in local pH.[18,56,57] Higher pH values favor the formation of a larger number of soluble Cu complexes, which contributes for accelerated corrosion in those microenvironment conditions (Figure 7). The formation of crevices in large, corroded Cu particles supports that the preferential corrosion of larger particles is linked to their higher defect density, which accelerates corrosion by facilitating a crevice corrosion mechanism. This contrasts, for example, with surface driven corrosion observed in Cu nanocubes with a surface oxide layer.[31] The number of macro- and micro-defects—initiation corrosion sites—correlates with particle size.[58] Electrochemical plating is eclipsed by corrosion through formation of soluble copper-CO_2-related complexes when a higher number of reactive sites is present. The enhanced corrosion of larger Cu particles and greater stability of small, re-plated particles observed in this study is contrary to thermodynamic stability theory predicting that larger particles are more stable and are expected to grow at the expense of small ones (Figure 2B).[59,60]

Copper corrosion appears slower at more negative potentials (Figures 2B vs. 5B), where (1) the cathodic field makes the formation of Cu and CO_2 related complexes less favorable, (2) surface Cu oxide species that facilitate the formation of Cu-CO_3 and Cu-HCO_3-type species are less stable, and (3) the direct interaction of negatively charged anions with the surface becomes unlikely.[42] Indeed, as observed in previous studies, the strong electrochemical driving force toward plating induces the formation of small re-plated copper particles observed at E_{WE} < 0 V (Figures 2B, 4B, and S8).[35,61–63]

These results are important as they lay out the mechanism and potential ways to mitigate copper degradation during CO_2 ER. Mitigation of this issue can likely benefit from strategies such as alloying or addition of inhibiting compounds, such as

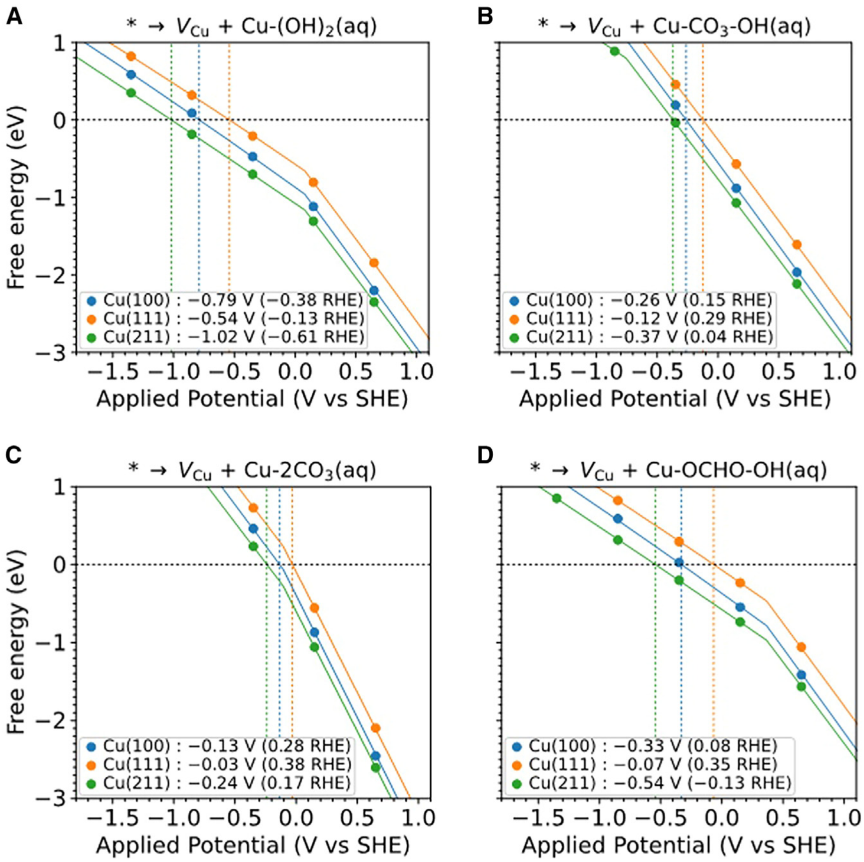

Figure 6. Calculated vacancy formation energies $E_F[V_{Cu}]$ on different Cu facets

(A) Cu-(OH)$_2$, (B) Cu-CO$_3$-OH, (C) Cu-2CO$_3$, and (D) Cu-OCHO-OH. The results are calculated for a pH of 7 and electrolyte ionic strength of 0.1M similar to that measured in the experiments. EF [VCu] shown as a function of applied potential vs. SHE. The dashed lines represent the thermodynamic oxidation/dissolution potential (Vdis) when EF[VCu] = 0 with the Cu chemical potential µCu determined from the copper species complex as denoted in the text, and are also included in the inset legends. We include the diagrams for the four most stable aqueous Cu complexes observed that are likely associated with CO2 reduction in HCO3-containing electrolytes. Additional details are included in the supplemental information.

surfactants, phosphates, or natural organic matter.[42,58,64] This study strongly suggests that small Cu catalysts (<25 nm), prepared *in situ* through electrodeposition, exhibit much greater stability during CO_2 ER than larger ones. In the near future, it would be very interesting to see a new study analyzing the stability of small, electroplated Cu particles, while simultaneously considering the effects on their catalytic activity. While CO_2-induced degradation can be mitigated, it is widely accepted that it cannot be fully stopped.[64,65]

Conclusions

In the presence of CO_2, copper degradation can proceed even if the applied electrochemical potential is not sufficient to drive CO_2 ER. When CO_2 is present in solution, copper and CO_2-containing species form soluble complexes. Copper degradation does not happen if $KHCO_3$ is present in solution without CO_2. *Ab initio* calculations show that surface copper species are prone to dissolution under modest reducing potentials in the presence of CO_2, most likely due to OCHO-containing complexes. Both our calculations and experimental measurements identify that Cu dissolution is exacerbated for oxidized surfaces that can lead to the formation of a larger number of soluble Cu complexes in the presence of CO_2. Copper degradation is disfavored at more negative electrochemical potentials, where a strong electrochemical driving force opposes the dissolution process. The enhanced propensity of larger copper particles to degrade is rationalized with exacerbated pH changes that

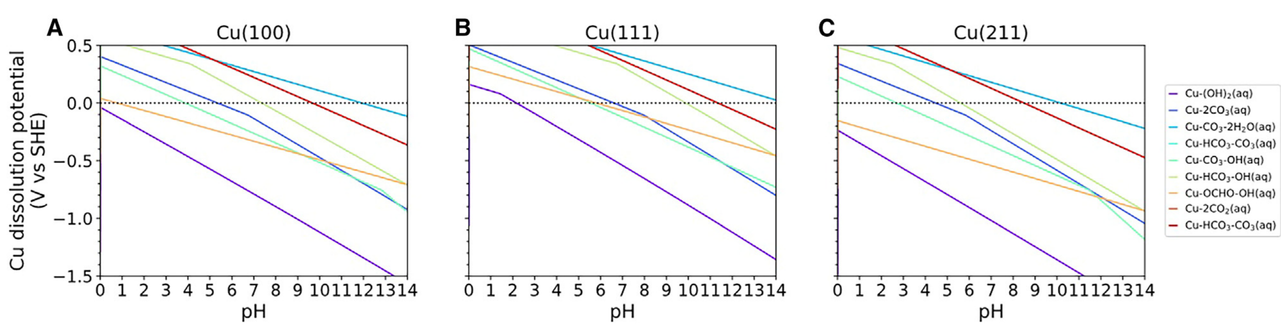

Figure 7. Calculated dissolution potential for V_{Cu} formation via different Cu complexes as a function of pH for different facets

(A) (100), (B) (111), and (C) (211) Cu facets. Potentials more reducing than the values shown for each complex indicate when the reaction becomes thermodynamically unfavorable, as seen in Figure 6. We include the diagrams for the four most stable aqueous Cu complexes observed that are likely associated with CO_2 reduction in HCO_3-containing electrolytes: (a) Cu-(OH)$_2$, (b) Cu-CO$_3$-OH, (c) Cu-2CO$_3$ and (d) Cu-OCHO-OH. The results are calculated for an electrolyte ionic strength of 0.1M and [Cu] as in Figure 6.

facilitate the formation of additional soluble copper complexes according to the DFT calculations.

Limitations of the study

Although significant efforts were made to mitigate the limitations of this study, some might still influence the results and their interpretation, such as: (1) beam induced effects on copper during CO_2 ER; (2) analysis of particles that might not be representative of the entire sample; (3) differences between the simulated particles and those studied in the experiments; (4) confinement effects due to the very reduced dimensions of the TEM electrochemical liquid cell.

RESOURCE AVAILABILITY

Lead contact

Requests for further information and resources should be directed to and will be fulfilled by the lead contact, Eric A. Stach (stach@seas.upenn.edu).

Materials availability

This study did not generate new unique reagents.

Data and code availability

- Raw data reported in this paper will be shared by the lead contact upon request.
- This paper does not report original code.
- Any additional information required to reanalyze the data reported in this paper is available from the lead contact upon request.

ACKNOWLEDGMENTS

The work was partially performed under the auspices of the U.S. Department of Energy by Lawrence Livermore National Laboratory under contract DE-AC52-07NA27344, and supported by the U.S. Department of Energy's Office of Energy Efficiency and Renewable Energy (EERE) under Advanced Manufacturing Office Next Generation R&D Projects award no. DE-EE-0008327. This work was carried out in part at the Singh Center for Nanotechnology at the University of Pennsylvania, which is supported by the NSF National Nanotechnology Coordinated Infrastructure Program under grant NNCI-2025608. Additional support to the Nanoscale Characterization Facility at the Singh Center has been provided by the Laboratory for Research on the Structure of Matter (MRSEC) supported by the U.S. National Science Foundation (DMR-1720530 and DMR-2309043). R.S.-M. thanks Net4CO2 Collaborative Laboratory (Porto, Portugal) - a Portuguese incubation laboratory dedicated to developing CO_2 capture and utilization and storage solutions - for supporting the costs of his trip and attendance to the Gordon Research Conference of Liquid Cell TEM 2022, where preliminary results of this study were presented, and valuable feedback was received.

AUTHOR CONTRIBUTIONS

R.S.-M. led and performed experimental studies and was the primary writer of the paper. J.B.V., S.E.W., H.Y., R.S., J.B., and S.A.A. performed ab initio simulations and contributed significantly to writing the paper. E.A.S. and S.A.A. conceived and designed the study. E.A.S., J.B., and S.A.A. supervised and ensured the implementation of self-assessment tests to improve the robustness of the methodology and revised the paper. All authors participated actively in monthly meetings to ensure consistency between experiments and simulations and improve their implementation throughout the project.

DECLARATION OF INTERESTS

The authors declare the following competing financial interest. Eric Stach is a co-founder of Hummingbird Scientific. Products manufactured by Hummingbird Scientific were utilized in the work. At the time of manuscript submission, he was also an equity holder and Chief Technology Officer. At the time of publication, he no longer retains equity or a role in the company.

STAR★METHODS

Detailed methods are provided in the online version of this paper and include the following:

- KEY RESOURCES TABLE
- METHOD DETAILS
  - Electrochemical TEM setup
  - Electrolyte preparation
  - Copper plating
  - CO_2 electroreduction tests
  - Morphological and chemical analysis
  - *Ab* initio calculations
- QUANTIFICATION AND STATISTICAL ANALYSIS

SUPPLEMENTAL INFORMATION

Supplemental information can be found online at https://doi.org/10.1016/j.isci.2025.111851.

Received: July 15, 2024
Revised: October 11, 2024
Accepted: January 16, 2025
Published: January 20, 2025

REFERENCES

1. Nocera, D.G. (2017). Solar fuels and solar chemicals industry. Accounts Chem. Res. *50*, 616–619.
2. Chu, S., and Majumdar, A. (2012). Opportunities and Challenges for a Sustainable Energy Future. Nature *488*, 294–303.
3. Our World in Data: Energy. https://doi.org/10.1016/ourworldindata.org/energy.
4. Stigka, E.K., Paravantis, J.A., and Mihalakakou, G.K. (2014). Social acceptance of renewable energy sources: A review of contingent valuation applications. Renew. Sustain. Energy Rev. *32*, 100–106.
5. Chu, S., Cui, Y., and Liu, N. (2016). The path towards sustainable energy. Nat. Mater. *16*, 16–22.
6. Serra-Maia, R., Michel, F.M., Douglas, T.A., Kang, Y., and Stach, E.A. (2021). Mechanism and Kinetics of Methane Oxidation to Methanol Catalyzed by AuPd Nanocatalysts at Low Temperature. ACS Catal. *11*, 2837–2845. https://doi.org/10.1021/acscatal.0c04487.
7. Kunene, T., Xiong, L., and Rosenthal, J. (2019). Solar-powered synthesis of hydrocarbons from carbon dioxide and water. Proc. Natl. Acad. Sci. USA *116*, 9693–9695.
8. Appel, A.M., Bercaw, J.E., Bocarsly, A.B., Dobbek, H., DuBois, D.L., Dupuis, M., Ferry, J.G., Fujita, E., Hille, R., Kenis, P.J.A., et al. (2013). Frontiers, opportunities, and challenges in biochemical and chemical catalysis of CO2 fixation. Chem. Rev. *113*, 6621–6658.
9. Kuhl, K.P., Hatsukade, T., Cave, E.R., Abram, D.N., Kibsgaard, J., and Jaramillo, T.F. (2014). Electrocatalytic conversion of carbon dioxide to methane and methanol on transition metal surfaces. J. Am. Chem. Soc. *136*, 14107–14113.
10. Zhu, Q., Sun, X., Yang, D., Ma, J., Kang, X., Zheng, L., Zhang, J., Wu, Z., and Han, B. (2019). Carbon dioxide electroreduction to C2 products over copper-cuprous oxide derived from electrosynthesized copper complex. Nat. Commun. *10*, 3851.
11. Snuffin, L.L., Whaley, L.W., and Yu, L. (2011). Catalytic electrochemical reduction of CO2 in ionic liquid EMIMBF3Cl. J. Electrochem. Soc. *158*, F155.

12. Dinh, C.-T., Burdyny, T., Kibria, M.G., Seifitokaldani, A., Gabardo, C.M., García de Arquer, F.P., Kiani, A., Edwards, J.P., De Luna, P., Bushuyev, O.S., et al. (2018). CO2 electroreduction to ethylene via hydroxide-mediated copper catalysis at an abrupt interface. Science *360*, 783–787.
13. Qiao, J., Liu, Y., and Zhang, J. (2016). Electrochemical Reduction of Carbon Dioxide: Fundamentals and Technologies (CRC press).
14. Prieto, G., De Mello, M.I.S., Concepción, P., Murciano, R., Pergher, S.B.C., and Martínez, A. (2015). Cobalt-catalyzed Fischer–Tropsch synthesis: chemical nature of the oxide support as a performance descriptor. ACS Catal. *5*, 3323–3335.
15. Speck, F.D., and Cherevko, S. (2020). Electrochemical copper dissolution: A benchmark for stable CO2 reduction on copper electrocatalysts. Electrochem. Commun. *115*, 106739. https://doi.org/10.1016/j.elecom.2020.106739.
16. Ren, D., Deng, Y., Handoko, A.D., Chen, C.S., Malkhandi, S., and Yeo, B.S. (2015). Selective electrochemical reduction of carbon dioxide to ethylene and ethanol on copper (I) oxide catalysts. ACS Catal. *5*, 2814–2821.
17. Chan, K. (2020). A few basic concepts in electrochemical carbon dioxide reduction. Nat. Commun. *11*, 5954.
18. Ooka, H., Figueiredo, M.C., and Koper, M.T.M. (2017). Competition between hydrogen evolution and carbon dioxide reduction on copper electrodes in mildly acidic media. Langmuir *33*, 9307–9313.
19. Chen, C.S., Handoko, A.D., Wan, J.H., Ma, L., Ren, D., and Yeo, B.S. (2015). Stable and selective electrochemical reduction of carbon dioxide to ethylene on copper mesocrystals. Catal. Sci. Technol. *5*, 161–168.
20. Popović, S., Nazrulla, M.A., Šket, P., Kamal, K.M., Likozar, B., Suhadolnik, L., Pavko, L., Surca, A.K., Bele, M., and Hodnik, N. (2022). Electrochemically-grown Chloride-free Cu2O nanocubes favorably electroreduce CO2 to Methane: The interplay of appropriate electrochemical protocol. Electrochim. Acta *436*, 141458. https://doi.org/10.1016/j.electacta.2022.141458.
21. Cheng, W.-H., Shiau, C.-Y., Hsieh Liu, T., Ling Tung, H., Hsu Chen, H., Lu, J.-F., and Cheng Hsu, C. (1998). Stability of copper based catalysts enhanced by carbon dioxide in methanol decomposition. Appl. Catal. B Environ. *18*, 63–70.
22. Hori, Y., Konishi, H., Futamura, T., Murata, A., Koga, O., Sakurai, H., and Oguma, K. (2005). "Deactivation of copper electrode" in electrochemical reduction of CO2. Electrochim. Acta *50*, 5354–5369.
23. Ramdin, M., De Mot, B., Morrison, A.R.T., Breugelmans, T., van den Broeke, L.J.P., Trusler, J.P.M., Kortlever, R., De Jong, W., Moultos, O.A., Xiao, P., et al. (2021). Electroreduction of CO2/CO to C2 products: process modeling, downstream separation, system integration, and economic analysis. Ind. Eng. Chem. Res. *60*, 17862–17880.
24. Moradzaman, M., Martínez, C.S., and Mul, G. (2020). Effect of partial pressure on product selectivity in Cu-catalyzed electrochemical reduction of CO 2. Sustain. Energy Fuels *4*, 5195–5202.
25. DeCiccio, D., Ahn, S., Sen, S., Schunk, F., Palmore, G., and Rose-Petruck, C. (2015). Electrochemical reduction of CO2 with clathrate hydrate electrolytes and copper foam electrodes. Electrochem. Commun. *52*, 13–16.
26. DeWulf, D.W., Jin, T., and Bard, A.J. (1989). Electrochemical and surface studies of carbon dioxide reduction to methane and ethylene at copper electrodes in aqueous solutions. J. Electrochem. Soc. *136*, 1686–1691.
27. Wasmus, S., Cattaneo, E., and Vielstich, W. (1990). Reduction of carbon dioxide to methane and ethene—an on-line MS study with rotating electrodes. Electrochim. Acta *35*, 771–775.
28. Kyriacou, G., and Anagnostopoulos, A. (1992). Electroreduction of CO2 on differently prepared copper electrodes: The influence of electrode treatment on the current efficiences. J. Electroanal. Chem. *322*, 233–246.
29. Osowiecki, W.T., Nussbaum, J.J., Kamat, G.A., Katsoukis, G., Ledendecker, M., Frei, H., Bell, A.T., and Alivisatos, A.P. (2019). Factors and dynamics of Cu nanocrystal reconstruction under CO2 reduction. ACS Appl. Energy Mater. *2*, 7744–7749.
30. Jung, H., Lee, S.Y., Lee, C.W., Cho, M.K., Won, D.H., Kim, C., Oh, H.-S., Min, B.K., and Hwang, Y.J. (2019). Electrochemical fragmentation of Cu2O nanoparticles enhancing selective C–C coupling from CO2 reduction reaction. J. Am. Chem. Soc. *141*, 4624–4633.
31. Liu, S., Li, Y., Wang, D., Xi, S., Xu, H., Wang, Y., Li, X., Zang, W., Liu, W., Su, M., et al. (2024). Alkali cation-induced cathodic corrosion in Cu electrocatalysts. Nat. Commun. *15*, 5080.
32. Huang, J., Hörmann, N., Oveisi, E., Loiudice, A., De Gregorio, G.L., Andreussi, O., Marzari, N., and Buonsanti, R. (2018). Potential-induced nanoclustering of metallic catalysts during electrochemical CO2 reduction. Nat. Commun. *9*, 3117.
33. Hodnik, N., Dehm, G., and Mayrhofer, K.J.J. (2016). Importance and challenges of electrochemical *in situ* liquid cell electron microscopy for energy conversion research. Acc. Chem. Res. *49*, 2015–2022.
34. Grosse, P., Gao, D., Scholten, F., Sinev, I., Mistry, H., and Roldan Cuenya, B. (2018). Dynamic changes in the structure, chemical state and catalytic selectivity of Cu nanocubes during CO2 electroreduction: size and support effects. Angew. Chem. *130*, 6300–6305.
35. Grosse, P., Yoon, A., Rettenmaier, C., Herzog, A., Chee, S.W., and Roldan Cuenya, B. (2021). Dynamic transformation of cubic copper catalysts during CO2 electroreduction and its impact on catalytic selectivity. Nat. Commun. *12*, 6736.
36. Grosse, P., Yoon, A., Rettenmaier, C., Chee, S.W., and Cuenya, B.R. (2020). Growth dynamics and processes governing the stability of electrodeposited size-controlled cubic Cu catalysts. J. Phys. Chem. C Nanomater. Interfaces *124*, 26908–26915.
37. Merola, C., Cheng, H.-W., Schwenzfeier, K., Kristiansen, K., Chen, Y.-J., Dobbs, H.A., Israelachvili, J.N., and Valtiner, M. (2017). In situ nano-to microscopic imaging and growth mechanism of electrochemical dissolution (eg, corrosion) of a confined metal surface. Proc. Natl. Acad. Sci. USA *114*, 9541–9546.
38. Engelbrecht, A., Uhlig, C., Stark, O., Hämmerle, M., Schmid, G., Magori, E., Wiesner-Fleischer, K., Fleischer, M., and Moos, R. (2018). On the Electrochemical CO2 Reduction at Copper Sheet Electrodes with Enhanced Long-Term Stability by Pulsed Electrolysis. J. Electrochem. Soc. *165*, J3059–J3068. https://doi.org/10.1149/2.0091815jes.
39. Garg, G., and Basu, S. (2015). Studies on Degradation of Copper Nano Particles in Cathode for CO2 Electrolysis to Organic Compounds. Electrochim. Acta *177*, 359–365. https://doi.org/10.1016/j.electacta.2015.03.161.
40. Myers, J.R., and Cohen, A. (1995). Pitting corrosion of copper in cold potable water systems. Mater. Perform. *34*, 60–62.
41. Lytle, D.A., and Schock, M.R. (2008). Pitting corrosion of copper in waters with high pH and low alkalinity. J. AWWA (Am. Water Works Assoc.) *100*, 115–129. https://doi.org/10.1002/j.1551-8833.2008.tb09586.x.
42. Sarver, E., and Edwards, M. (2012). Inhibition of copper pitting corrosion in aggressive potable waters. Int. J. Corrosion *2012*, 1–16.
43. Lytle, D.A., Williams, D., and White, C. (2012). A simple approach to assessing copper pitting corrosion tendencies and developing control strategies. J. Water Supply Res. Technol. - Aqua *61*, 164–175. https://doi.org/10.2166/aqua.2012.079.
44. Nassiri, Y., Mansot, J.L., Wéry, J., Ginsburger-Vogel, T., and Amiard, J.C. (1997). Ultrastructural and electron energy loss spectroscopy studies of sequestration mechanisms of Cd and Cu in the marine diatom Skeletonema costatum. Arch. Environ. Contam. Toxicol. *33*, 147–155.
45. Laffont, L., Wu, M.Y., Chevallier, F., Poizot, P., Morcrette, M., and Tarascon, J.M. (2006). High resolution EELS of Cu–V oxides: Application to batteries materials. Micron *37*, 459–464. https://doi.org/10.1016/j.micron.2005.11.007.
46. Feaster, J.T., Shi, C., Cave, E.R., Hatsukade, T., Abram, D.N., Kuhl, K.P., Hahn, C., Nørskov, J.K., and Jaramillo, T.F. (2017). Understanding selectivity for the electrochemical reduction of carbon dioxide to formic acid and carbon monoxide on metal electrodes. ACS Catal. *7*, 4822–4827.

47. Ye, Y., Yang, H., Qian, J., Su, H., Lee, K.-J., Cheng, T., Xiao, H., Yano, J., Goddard, W.A., and Crumlin, E.J. (2019). Dramatic differences in carbon dioxide adsorption and initial steps of reduction between silver and copper. Nat. Commun. *10*, 1875.

48. Wang, S., Kou, T., Varley, J.B., Akhade, S.A., Weitzner, S.E., Baker, S.E., Duoss, E.B., and Li, Y. (2021). Cu2O/CuS Nanocomposites Show Excellent Selectivity and Stability for Formate Generation via Electrochemical Reduction of Carbon Dioxide. ACS Mater. Lett. *3*, 100–109. https://doi.org/10.1021/acsmaterialslett.0c00520.

49. Fan, L., Xia, C., Yang, F., Wang, J., Wang, H., and Lu, Y. (2020). Strategies in catalysts and electrolyzer design for electrochemical CO2 reduction toward C2+ products. Sci. Adv. *6*, eaay3111.

50. Simon, G.H., Kley, C.S., and Roldan Cuenya, B. (2021). Potential-Dependent Morphology of Copper Catalysts During CO2 Electroreduction Revealed by In Situ Atomic Force Microscopy. Angew. Chem., Int. Ed. Engl. *60*, 2561–2568. https://doi.org/10.1002/anie.202010449.

51. Arán-Ais, R.M., Rizo, R., Grosse, P., Algara-Siller, G., Dembélé, K., Plodinec, M., Lunkenbein, T., Chee, S.W., and Cuenya, B.R. (2020). Imaging electrochemically synthesized Cu2O cubes and their morphological evolution under conditions relevant to CO2 electroreduction. Nat. Commun. *11*, 3489. https://doi.org/10.1038/s41467-020-17220-6.

52. Knurr, B.J., and Weber, J.M. (2014). Structural Diversity of Copper–CO2 Complexes: Infrared Spectra and Structures of [Cu(CO2)n]− Clusters. J. Phys. Chem. A *118*, 10246–10251. https://doi.org/10.1021/jp508219y.

53. Agnelli, M., Grandia, F., Soler, D., Sáinz-García, A., Brusi, D., Zamorano, M., and Menció, A. (2018). Metal release in shallow aquifers impacted by deep CO2 fluxes. Energy Proc. *146*, 38–46.

54. Livingston, R.A. (2016). Acid rain attack on outdoor sculpture in perspective. Atmos. Environ. *146*, 332–345.

55. Mehta, P. (2010). Science behind acid rain: analysis of its impacts and advantages on life and heritage structures. S. Asian J. Tour. Herit. *3*, 123–132.

56. Goyal, A., Marcandalli, G., Mints, V.A., and Koper, M.T.M. (2020). Competition between CO2 reduction and hydrogen evolution on a gold electrode under well-defined mass transport conditions. J. Am. Chem. Soc. *142*, 4154–4161.

57. Raciti, D., Mao, M., Park, J.H., and Wang, C. (2018). Local pH effect in the CO2 reduction reaction on high-surface-area copper electrocatalysts. J. Electrochem. Soc. *165*, F799–F804.

58. Zhang, B., and Ma, X. (2019). A review—Pitting corrosion initiation investigated by TEM. J. Mater. Sci. Technol. *35*, 1455–1465.

59. Boita, J., Nicolao, L., Alves, M.C.M., and Morais, J. (2017). Controlled growth of metallic copper nanoparticles. New J. Chem. *41*, 14478–14485.

60. Li, M., Borsay, A., Dakhchoune, M., Zhao, K., Luo, W., and Züttel, A. (2020). Thermal stability of size-selected copper nanoparticles: Effect of size, support and CO2 hydrogenation atmosphere. Appl. Surf. Sci. *510*, 145439.

61. Yang, Y., Louisia, S., Yu, S., Jin, J., Roh, I., Chen, C., Fonseca Guzman, M.V., Feijóo, J., Chen, P.-C., Wang, H., et al. (2023). Operando studies reveal active Cu nanograins for CO2 electroreduction. Nature *614*, 262–269.

62. Vavra, J., Ramona, G.P.L., Dattila, F., Kormányos, A., Priamushko, T., Albertini, P.P., Loiudice, A., Cherevko, S., Lopéz, N., and Buonsanti, R. (2024). Solution-based Cu+ transient species mediate the reconstruction of copper electrocatalysts for CO2 reduction. Nat. Catal. *7*, 89–97.

63. Zhang, Q., Song, Z., Sun, X., Liu, Y., Wan, J., Betzler, S.B., Zheng, Q., Shangguan, J., Bustillo, K.C., Ercius, P., et al. (2024). Atomic dynamics of electrified solid–liquid interfaces in liquid-cell TEM. Nature *630*, 643–647. https://doi.org/10.1038/s41586-024-07479-w.

64. Usman, B.J., and Ali, S.A. (2018). Carbon dioxide corrosion inhibitors: a review. Arabian J. Sci. Eng. *43*, 1–22.

65. Brondel, D., Montrouge, F., Edwards, R., Hayman, A., Hill, D., Mehta, S., and Semerad, T. (1987). Corrosion in the oil industry. J. Petrol. Technol. *39*, 756–762.

66. Karki, K., Serra-Maia, R., Stach, E., Alsem, D.H., and Salmon, N. (2020). Realistic Bulk Electrochemistry in Liquid Cell Microscopy. Microsc. Microanal. *26*, 1458–1459.

67. Serra-Maia, R., Kumar, P., Meng, A.C., Foucher, A.C., Kang, Y., Karki, K., Jariwala, D., and Stach, E.A. (2021). Nanoscale chemical and structural analysis during *in situ* scanning/transmission electron microscopy in liquids. ACS Nano *15*, 10228–10240.

68. Quezada, D., Honores, J., García, M., Armijo, F., and Isaacs, M. (2014). Electrocatalytic reduction of carbon dioxide on a cobalt tetrakis (4-aminophenyl) porphyrin modified electrode in BMImBF 4. New J. Chem. *38*, 3606–3612.

69. Gu, M., Parent, L.R., Mehdi, B.L., Unocic, R.R., McDowell, M.T., Sacci, R.L., Xu, W., Connell, J.G., Xu, P., Abellan, P., et al. (2013). Demonstration of an electrochemical liquid cell for operando transmission electron microscopy observation of the lithiation/delithiation behavior of Si nanowire battery anodes. Nano Lett. *13*, 6106–6112.

70. de Jonge, N. (2018). Theory of the spatial resolution of (scanning) transmission electron microscopy in liquid water or ice layers. Ultramicroscopy *187*, 113–125.

71. de Jonge, N., Verch, A., and Demers, H. (2018). The influence of beam broadening on the spatial resolution of annular dark field scanning transmission electron microscopy. Microsc. Microanal. *24*, 8–16.

72. Jungjohann, K.L., Evans, J.E., Aguiar, J.A., Arslan, I., and Browning, N.D. (2012). Atomic-scale imaging and spectroscopy for *in situ* liquid scanning transmission electron microscopy. Microsc. Microanal. *18*, 621–627.

73. Holtz, M.E., Yu, Y., Gao, J., Abruña, H.D., and Muller, D.A. (2013). In situ electron energy-loss spectroscopy in liquids. Microsc. Microanal. *19*, 1027–1035.

74. Woehl, T.J., Moser, T., Evans, J.E., and Ross, F.M. (2020). Electron-beam-driven chemical processes during liquid phase transmission electron microscopy. MRS Bull. *45*, 746–753. https://doi.org/10.1557/mrs.2020.227.

75. Hammer, B., Hansen, L.B., and Nørskov, J.K. (1999). Improved adsorption energetics within density-functional theory using revised Perdew-Burke-Ernzerhof functionals. Phys. Rev. B *59*, 7413–7421.

76. Mathew, K., Sundararaman, R., Letchworth-Weaver, K., Arias, T.A., and Hennig, R.G. (2014). Implicit solvation model for density-functional study of nanocrystal surfaces and reaction pathways. J. Chem. Phys. *140*, 084106.

77. Duan, Z., and Xiao, P. (2021). Simulation of Potential-Dependent Activation Energies in Electrocatalysis: Mechanism of O–O Bond Formation on RuO2. J. Phys. Chem. C *125*, 15243–15250.

STAR★METHODS

KEY RESOURCES TABLE

REAGENT or RESOURCE	SOURCE	IDENTIFIER
Software and algorithms		
VASP	University of Anytown	**VASP**.6.3.1
Gatan Digital Micrograph	Gatan Ametek	**Digital Micrograph** Version 3.60.4441.0
Other		
Electrochemical sample holder	Hummingbird Scientific	Gen II Liquid Cell TEM Holder

METHOD DETAILS

Electrochemical TEM setup

This study was performed using TEM cells assembled with parts supplied by Hummingbird Scientific (USA). The assembled cell consists of two silicon-based chips and two O-rings that are sandwiched together to enclose the electrolyte flow path, as described in detail before.[66,67] One chip (electroactive chip) contains patterned electrodes, while the other (spacer) contains patterned posts that dictate the spacing between the electroactive chip and the spacer. Both chips have an electron beam transparent Si_xN_y window aligned with each other. The chip side with patterned electrodes is laid facing the spacing posts on the spacer chip, thus creating an enclosed liquid-cell. In the present study the electroactive chip was patterned with four separate electrodes that could be wired in the desired configuration. Three of the electrodes were made of platinum and one was made of amorphous indium tin oxide (ITO). The ITO electrode was used as the working electrode in all experiments. This electrode was patterned partially over the Si_xN_y window, which is key for performing TEM analysis on the copper particles. The sample holder was assembled with the electroactive chip on the side closest to the electron gun inside the TEM, which allows obtaining optimal resolution in STEM mode. In this orientation, the STEM electron probe reaches the sample at its smallest diameter before crossing and scattering through the thick column of electrolyte liquid.[67]

The cell is mounted on a liquid sample holder (Hummingbird Scientific, USA). The sample holder has four leads that establish electrical connection with up to four electrodes of the top, electroactive chip. The chip electrodes can be wired in any desired configuration. Amorphous ITO was used as the working electrode (WE), while the counter (CE) and pseudo-reference electrodes (RE) were made of platinum to ensure good conductivity. A three-electrode configuration was used in all experiments. Amorphous ITO film is inert for CO_2 ER and HER, which ensures that all the detected activity was from the copper catalyst deposited *in situ* for the experiments reported here (Figure S1).[68] The only exception to this configuration was for bulk copper corrosion analysis, where the WE was a copper electrode prepared by the supplier through e-beam deposition during chip manufacture.

Electrolyte preparation

Copper plating was performed using 0.01 mol/L $CuSO_4$. The $CuSO_4$ electrolyte was prepared freshly from $CuSO_4.5H_2O$ powder (Sigma Aldrich, USA). Liquid electrolyte solutions of 0.01 or 0.1 mol/L $KHCO_3$ or K_2SO_4 were used for the CO_2 ER experiments. The electrolytes were prepared from dry powders immediately before each experiment (Sigma Aldrich, USA). The electrolyte was saturated with CO_2 or N_2, prior their use for CO_2 ER experiments, through continuous vigorous bubbling at ambient conditions for >1 h.[35–37] Electrolyte was drawn directly into a syringe from the N_2- or CO_2-saturated solution and immediately pumped into the electrochemical cell at 10 μL/min, which pushed out the 0.01 M $CuSO_4$ used during copper electroplating thus filling the electrochemical cell with the CO_2 ER electrolyte.

Copper plating

Copper catalyst was electrodeposited from a 0.01 M $CuSO_4$ at E_{WE} = 0 V vs SHE' for 10s followed by E_{WE} = 0.15 V vs. SHE' for 1 min. Once the copper catalyst was plated onto the electrode, the electric current of the WE was held constant at 0 nA using the potentiostat to prevent any additional electrochemical changes to the catalyst. Morphological analysis of the catalyst in the original condition was performed at this point. Subsequently, the electrolyte was exchanged to $KHCO_3$ or K_2SO_4 for the CO_2 ER copper degradation analysis. The required volume of electrolyte for a complete exchange was determined through preliminary tests, which established the amount of electrolyte needed to reach the specimen chamber through the leading electrolyte lines. Complete electrolyte exchange was further ensured *in situ* for each experiment. The electrolyte exchange was performed at zero current. To maintain zero current, the potentiostat counterbalanced the open-circuit potential. Hence, the corresponding change of E_{WE} during the electrolyte exchange allowed ensuring that the process was complete before CO2 ER tests were initiated. Figure S2 shows a typical E_{WE} vs t curve observed during the electrolyte exchange process.

CO_2 electroreduction tests

All CO_2 ER experiments were performed with a research-grade BioLogic SP-150 potentiostat (BioLogic, USA) with ultra-low-current capability (76 fA current resolution). The electrolyte concentration was 0.01 mol/L, unless otherwise stated. The electrochemical cell was prepared using the set-up developed before for Transmission Electron Microscopy (TEM) electrochemical experiments.[67] In summary both chips were first plasma treated with Argon and the cell was primed with 0.01 mol/L $CuSO_4$ electrolyte at a flow rate of 20 μL/min before inserting into the TEM. Confirmation that the cell had effectively filled with $CuSO_4$ electrolyte was done by observing the cell area under an optical microscope. Once the electrolyte filled the cell entirely, the sample holder was introduced into the TEM. For this step, the electrolyte flow was lowered to 2 μL/min and all electrical connections remained disconnected to ensure that no electrochemical reactions could occur induced by electric fields in the TEM. The electrical connections of the sample holder were then established, while the potentiostat was used to impose 0 nA at the WE and the CE was electrically shorted to the goniometer to prevent adventitious electric currents between the electrodes and the cell cage. The experimental electrochemical potentials were calibrated by comparing the measured $CuSO_4$/Cu electrochemical potential with the standard hydrogen potential for that redox pair (Figure S3). The calibrated experimental potentials were identified as SHE'.

The $KHCO_3$ or K_2SO_4 solutions that had been pre-saturated with CO_2 or N_2 were introduced into the electrochemical cell at a flow rate of 10 μL/min to minimize the time it took to exchange $CuSO_4$ to $KHCO_3$ or K_2SO_4 in the electrochemical cell. Once the pre-saturated $KHCO_3$ or K_2SO_4 electrolyte reached the cell, the CO_2 ER protocol was initiated by fixing E_{WE} at the desired value. E_{WE} was maintained constant during the entire experiment. All experiments in this study were performed at pH values ranging from 5 to 7 to exclude Cu corrosion by too low or too high pH values. Nevertheless, local pH changes, for example under locally confined conditions like those found in crevice corrosion, could still happen.

Morphological and chemical analysis

Morphological analysis of the deposited copper electrocatalyst was performed through Scanning/Transmission Electron Microscopy using a JEOL F200 microscope operating at an acceleration voltage of 200 kV. The measured STEM resolution for the instrument is 0.136 nm. Imaging was performed in BF-STEM mode due to better resolution in liquids.[67,69–73] Imaging was performed using a probe size of 7, coupled with a 40 mm condenser aperture, which resulted in an approximate probe current of 60 pA. The catalyst was analyzed at select experimental times to avoid beam induced damage imparted from continuous beam irradiation effects in liquid conditions.[67,74] The raw images were processed with Gatan Digital Micrograph software.

To perform chemical and oxidation state analysis, at the end of the CO_2 ER experiments the cell was flushed with nitrogen and transferred to the instrument with EELS capabilities. The dry chip with patterned electrode and copper catalyst was then analyzed through Electron Energy Loss Spectroscopy (EELS) using a Gatan Ultrascan detector on a JEOL NEOARM microscope operating at 200 kV. The spectra were collected with a Gatan imaging filter (GIF) aperture of 2.5 mm and a collection semi-angle of β of 41.7 mrad using a 6C probe size with 0.025 eV of energy dispersion at a 20 mm camera length. Zero-loss and core-loss spectra were obtained using an exposure of 2×10^{-5} s and 5 s, respectively. Processing of EELS signal was performed using Origin Pro.

Ab initio calculations

All calculations were carried out using the Vienna Ab initio Simulation Package (VASP) code and the projector-augmented wave (PAW) technique using the RPBE exchange-correlation functional.[75] Constant voltage calculations were performed using the VASPsol implicit solvation method, assuming an SHE reference of –4.45 eV relative to the vacuum level.[15,76,77] This approach implements an embedded polarizable dielectric continuum model that treats the ionic countercharge using a linearized Poisson-Boltzmann distribution. All calculations were performed using a dielectric constant of 80, a Debye length of 3 Å, and neglecting the cavitation energy contribution. All copper slab calculations were done using low-index copper surfaces of Cu (100), Cu (111) and Cu (211) with a vacuum region of 20 Å and a cutoff energy of 500 eV for planewaves. Slab sizes were 4x4x4 for Cu(100), 4x4x3 for Cu(111), and 6x3x4 for Cu(211). The free energies were determined using calculated electronic energies for all species, assuming adsorbate and gas phase entropic adjustments. Further details can be found in the supplemental information.

To assess the degradation mechanisms, we evaluated the oxidation/dissolution potential (U_{dis}) of copper by computing the copper vacancy (V_{Cu}) formation energies ($E^f[V_{Cu}]$) as a function of applied potential, with the U_{dis} attributed to the potential at which the reaction becomes endergonic for a given surface facet. Specifically, we calculate the formation energy (or analogously the Cu dissolution energy) via the expression:

$$E^f\,[V_{Cu,}\,](\mu_e) = \Omega[\mathrm{Cu}(hkl){:}V_{Cu}](\mu_e) + \mu_{Cu}(\mu_e) - \Omega[\mathrm{Cu}(hkl)](\mu_e),$$

where Ω represents the electronic grand potential for the pristine slab ($\Omega[\mathrm{Cu}(hkl)]$) and the slab with a vacancy ($\Omega[\mathrm{Cu}(hkl){:}V_{Cu}]$), and μ_{Cu} represents the chemical potential of the oxidized Cu atom dissolved in solution. In this expression, all quantities are a function of the electron chemical potential, μ_e, which is related to the applied potential via the expression $U(\mu_e) = V(\mu_e) - V_{SHE}$, where $V(\mu_e) = -\mu_e/e_0$ and V_{SHE} is the SHE reference potential. The dissolution potential U_{dis} is computed by setting $E^f\,[V_{Cu,}\,](\mu_e) = 0$, which is associated with the electron chemical potential at which the pristine surface is in thermodynamic equilibrium with the dissolved Cu species and defective surface:

$$\Omega[\mathrm{Cu}(hkl)](U_{dis}) = \Omega[\mathrm{Cu}(hkl){:}V_{Cu}](U_{dis}) + \mu_{Cu}(U_{dis})$$

Within this framework, the dissolution potential is dependent upon two key factors: 1) the orientation of the Cu surface and 2) the nature of the dissolved Cu complex. The latter leads to variations in μ_{Cu}, which is highly dependent upon both the chemistry and the net charge of the complex. In this work, we have considered a diverse set of possible Cu complex ion chemistries by systematically replacing one or more water ligands in known aqua ion complex geometries with CO_2, CO_3, HCO_3, OH, and OCHO ligands. We refer the reader to the supplemental information for details of the structures for the studied Cu complexes. The μ_{Cu} for the different Cu complexes were calculated by subtracting off all energy contributions of the isolated constituents apart from Cu. For instance, the chemical potential of the copper-carbonate complex with a solvation shell of 2 H_2O molecules was calculated as follows:

$$\mu_{Cu} = G[\text{Cu-CO}_3\text{-2 H}_2\text{O}_{\ (aq)}] - G[\text{CO}_{3\ (aq)}] - 2\, G[\text{H}_2\text{O}_{\ (aq)}]$$

where $G[X_{\ (aq)}]$ represents the potential-dependent grand potential energy including vibrational corrections as described in the supplemental information. All energies were calculated using implicit solvation with potential control using the VASPsol code, with additional details included in the supplemental information. We note that the absolute values of chemical potential of the complex μ_{Cu} and $E^f[V_{Cu}]$ are modulated by details of the DFT calculations (*e.g.*, the exchange correlation functional) and the degree of solvation in the models (for instance, secondary solvation shell inclusion, *etc.*), and therefore the computational results primarily serve to provide quantitative insight and qualitative trends. The present study focuses on thermodynamic trends in comparison with experimental observations, but does not account for possible kinetic effects.

QUANTIFICATION AND STATISTICAL ANALYSIS

There are no quantification or statistical analyses to include in this study.